Article

Aging Behaviour of a 12.2Cr-10Ni-1Mo-1Ti-0.6Al Precipitation-Hardening Stainless Steel Manufactured via Laser Powder Bed Fusion

Alessandro Morri [1], Mattia Zanni [1,*], Lorella Ceschini [1], Alessandro Fortunato [1] and Massimo Pellizzari [2]

[1] Department of Industrial Engineering (DIN), Alma Mater Studiorum—University of Bologna, Viale Risorgimento 4, 40136 Bologna, Italy
[2] Department of Industrial Engineering, University of Trento, Via Sommarive 9, 38123 Trento, Italy
* Correspondence: mattia.zanni2@unibo.it

Abstract: The combination of precipitation-hardening stainless steels (PH-SS) and laser powder bed fusion (LPBF) enables the manufacturing of tools for plastic injection moulding with optimised geometry and conformal cooling channels, with potential benefits in terms of productivity, part quality, and tool duration. Moreover, the suitability of LPBF-manufactured PH-SS in the as-built (AB) condition to be age-hardened through a direct aging (DA) treatment enables a great heat treatment simplification with respect to the traditional solution annealing and aging treatment (SA). However, plastic injection moulding tools experience severe thermal cycles during their service, which can lead to over-aging of PH-SS and thus shorten tool life. Therefore, proper thermal stability is required to ensure adequate tool life and reliability. The aim of the present work is to investigate the aging and over-aging behaviour of a commercially available PH-SS (AMPO M789) manufactured by LPBF in the AB condition and after a solution-annealing treatment in order to evaluate the effect of the heat treatment condition on the microstructure and the aging and over-aging response, aiming at assessing its feasibility for plastic injection moulding applications. The AB microstructure features melt pool borders, oriented martensite grains, and a cellular solidification sub-structure, and was retained during aging and over-aging. On the other hand, a homogeneous and isotropic martensite structure was present after solution annealing and quenching, with no melt pool borders, cellular structure, or oriented grains. The results indicate no significant difference between AB and solution-annealed and quenched specimens in terms of aging and over-aging behaviour and peak hardness (in the range 580–600 HV), despite the considerably different microstructures. Over-aging was attributed to both the coarsening of strengthening precipitates and martensite-to-austenite reversion (up to ~11 vol.%) upon prolonged exposure to high temperature. Based on the results, guidelines to aid the selection of the most suitable heat treatment procedure are proposed.

Keywords: additive manufacturing; precipitation-hardening stainless steel; laser powder bed fusion; direct aging; over-aging

1. Introduction

Martensitic precipitation-hardening stainless steels (PH-SS) feature a favourable combination of mechanical strength, fracture toughness, and corrosion resistance, which make them suitable for tooling applications, mainly for dies for plastic injection moulding [1,2]. As for other precipitation-strengthened alloys, such as maraging (martensite-aging) steels, age-hardenable aluminium alloys, and Ni-based superalloys, the high hardness and strength of PH-SS come from the precipitation of nanometric intermetallic particles during heat treatment, which strengthen the matrix by lattice coherency strains or the Ashby or Orowan mechanism based on the precipitate–matrix characteristics [3]. The typical precipitation heat treatment of maraging and PH-SS, solution annealing and aging (SA), involves solution annealing in the austenite field (between 800 and 1040 °C according to the steel

composition), followed by rapid cooling and an aging step at a relatively low temperature (in the range of 480–600 °C), during which strengthening phases precipitate in a controlled fashion. The low-carbon Fe-Cr-Ni martensite formed after rapid cooling in martensitic PH-SS (annealed condition "A" according to ASTM A564) is relatively soft (approximatively 30 HRC), ductile, and tough, due to the low C content and lack of strengthening precipitates [1,2,4–6]. Martensitic PH-SS and maraging steels feature the same strengthening mechanisms (precipitation upon aging of a super-saturated low-C martensite) but typically different alloying elements and resulting properties. The most used PH-SS, Cu-bearing 17–4 PH and 15–5 PH, feature a high Cr content (14–17 wt.%) to ensure great corrosion resistance, sufficient Ni (3–5 wt.%) to avoid δ-ferrite formation during solution annealing by expanding the γ-austenite phase field (δ-ferrite reduces both corrosion resistance and mechanical properties), and 3–5 wt.% Cu to precipitate strengthening compounds upon aging. In the peak-aged condition (H900 temper), they exhibit a tensile strength around 1300 MPa with an elongation at fracture of roughly 10% [2,4]. On the opposite, maraging steels typically contain no Cr but high Ni (around 18 wt.%), 3–5 wt.% Mo and Ti to form Ni-based strengthening intermetallic compounds upon aging, and high Co (8–12 wt.%) to raise martensite formation temperatures sufficiently to avoid retained austenite after quenching. As a result, in H900 temper (peak aging) they exhibit considerably higher tensile strengths than Cu-bearing PH-SS, ranging from 1500 MPa for 18-Ni200 to 2000 MPa for 18-Ni300, with elongations in the range of 7–10%, in conjunction with a very high fracture toughness. However, maraging steels are not corrosion resistant due to the absence of Cr [6]. An intermediate class of steels between Cu-bearing PH-SS and maraging steels is represented by PH 13–8 Mo and similar, developed with the aim of maximising the mechanical properties of PH-SS while retaining adequate corrosion resistance. Usually, these steels are classified among PH-SS due to the relevant Cr content (around 13 wt.%, but lower than 17–4 PH and 15–5 PH). However, strengthening involves Ni-based precipitates; hence, they contain high Ni (8–10 wt.%) together with Ti and/or Al, which take part in precipitation reactions with Ni. Mo is added to improve the corrosion resistance by raising the thermodynamic activity of Cr and/or to avoid eventual embrittlement at the aging temperatures. PH 13–8 Mo and similar steels developed from it do not generally contain Cu or Co. The outcome is a combination of high mechanical strength, between that of Cu-bearing PH-SS and maraging steels depending on the steel composition, and adequate corrosion resistance [1,2,4,6]. Due to the overlapping characteristics, PH 13-8 Mo and similar steels are sometimes indicated as Co-free or corrosion-resistant maraging steels, despite the considerably different composition.

Precipitation-strengthened alloys usually face a hardness and strength decay upon prolonged exposure at high temperature (indicated as over-aging) due to the coarsening of strengthening precipitates, with the consequent loss of lattice coherency and transformation in equilibrium phases [3]. Over-aging is particularly relevant for aluminium alloys used for pistons and cylinder heads in internal combustion engines and Ni-based superalloys for turbine blades in energy generation applications. However, tools for plastic injection moulding also experience severe thermal cycles during their service operations, so the over-aging behaviour of PH-SS intended for tooling applications must be carefully evaluated to ensure proper life and reliability. Moreover, although precipitation-strengthened alloys are generally aged at peak hardness, over-aging can be deliberately induced during heat treatment for specific applications by adjusting the aging temperature and time. For example, age-hardened aluminium alloys can be treated to T7 temper to enhance dimensional and mechanical stability during the subsequent service [7]. In the case of PH-SS, over-aging can be exploited to achieve a required trade-off between strength and toughness [4].

Laser powder bed fusion (LPBF), also known as selective laser melting (SLM) or laser-based powder bed fusion (LB-PBF), according to ISO/ASTM 52900:2021, is a layer-by-layer additive manufacturing (AM) process that enables the design and production of components with complex shapes not obtainable via conventional techniques [8–11]. For tooling applications it enables the design and manufacturing of dies and inserts with

conformal cooling channels with increased cooling efficiency, leading to higher productivity and part surface quality [12–15]. PH-SS are easily manufacturable by LPBF due to their low C content, leading to a reduced risk of crack formation [14,16–18]. The as-built (AB) microstructure of LPBF-manufactured PH-SS consists of melt pool/scan track boundaries, a martensite microstructure with oriented grains, and a cellular solidification sub-structure, and exhibits relatively low hardness and strength due to the lack of strengthening precipitates comparable to condition A for conventionally manufactured PH-SS [8,14,17,19–30]. The AB microstructure of Cu-bearing 17–4 PH and 15–5 PH steels can possess significant amounts of metastable, retained γ-austenite, depending on the powder atomisation and LPBF inert gas atmosphere [18,31–40]. On the other hand, the AB structure of PH-SS, with a composition similar to PH 13-8 Mo (for example, stainless steels CX, Corrax, and M789, such as the one investigated in the present work), is inherently martensitic, with only low amounts of retained austenite [14,16–20,22,23,25,41,42]. Moreover, LPBF-manufactured PH-SS can be strengthened by a direct aging treatment (DA), with no solution annealing, due to the martensite microstructure with high alloying supersaturation in the AB condition resulting from the extremely high cooling rates of the LPBF process [19,22,29,43]. DA is also applied to other LPBF-manufactured precipitation-strengthened alloys, such as aluminium alloys (T5 temper) and maraging steels. DA is a promising heat treatment procedure for LPBF-manufactured PH-SS since it enables heat treatment simplification, energy saving, and cost and carbon footprint reduction by eliminating the solution-annealing and quenching steps. Moreover, it eliminates the risk of distortions and cracking during rapid cooling after solution annealing. However, DA preserves the main microstructural features of AB parts (melt pool boundaries, oriented grain structure, cellular solidification sub-structure).

The aim of the present work is to investigate the aging and over-aging behaviour of a 12.2Cr-10Ni-1Mo-1Ti-0.6Al PH-SS (AMPO M789) manufactured via LPBF in order to assess its feasibility for applications involving prolonged service at high temperature—for example, in dies for plastic injection moulding. The effect of different microstructures resulting from the application or not of a solution-annealing heat treatment was investigated. The behaviour of the steel was studied by performing aging and over-aging tests at various temperatures and durations and measuring the resulting hardness, considered representative of mechanical strength. Microstructural, dilatometric, and thermal analyses were performed with the aim of understanding the underlying mechanisms of aging and over-aging.
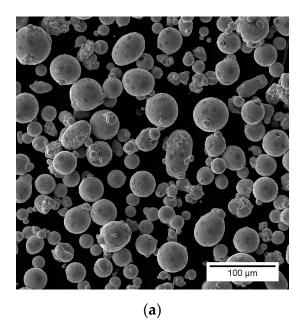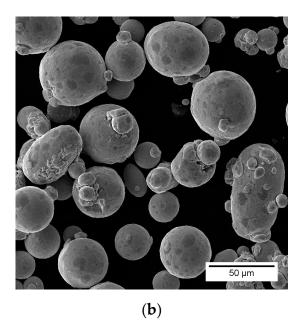
2. Materials and Methods

Specimens investigated in the present work were produced from the AMPO M789 feedstock powder supplied by Böhler Edelstahl (Kapfenberg, Austria) [44]. AMPO M789 is a PH-SS with proprietary composition from Böhler Edelstahl reported in Table 1 (nominal composition of the feedstock powder). Although it does not have direct matchings with existing steels defined in the main standards, it features a composition similar to PH 13–8 Mo, CX, and Corrax stainless steels, investigated in [14,19,20,22,23,30,41]. As previously described in the Introduction section, these steels are reinforced via Ni-rich precipitates and hence are sometimes indicated as Co-free maraging steels. The feedstock powder morphology, assessed using a Tescan Mira 3 field emission scanning electron microscope (SEM, TESCAN ORSAY Holding, Brno, Czech Republic) equipped with X-ray energy dispersive spectroscopy (EDS, Bruker Nano GmbH, Berlin, Germany) and electron back scattered diffraction (EBSD, Bruker Nano GmbH, Berlin, Germany), is reported in the representative micrographs in Figure 1. The largest fraction of particles exhibited a nearly spherical and regular morphology, although some elongated or irregular particles featuring small satellites were present. Specimens were manufactured using a SISMA MySint300 LPBF machine (SISMA, Vicenza, Italy) under a high-purity N_2 atmosphere with the following process parameters: laser power P = 250 W, scanning speed v = 800 mm/s, hatch spacing h = 0.1 mm, and layer thickness t = 30 μm. A 3 × 3 mm^2 island scan strategy was adopted.

Cylindrical bars (ø 13 × 130 mm^2) were manufactured with their longitudinal axis parallel to the vertical building direction (90° orientation), from which ø 13 × 4 mm^2 and ø 4 × 10 mm^2 samples were cut via wire electro discharge machining. Table 1 reports the effective composition of the feedstock powder and LPBF-manufactured samples evaluated via inductively coupled plasma–optical emission spectroscopy (ICP-OES, Thermo Fisher, Waltham, Massachusetts, U.S. for powders) and glow discharge–optical emission spectroscopy (GD-OES, Spectruma Analytik GmbH, Fabrikzeile, Germany, for LPBF samples) compared to the nominal one declared by the supplier of the feedstock powder. After production, part of the samples was solution annealed at 925 °C for 15 min followed by water quenching (S condition), whereas the rest was kept for direct aging from the as-built condition (AB).

Table 1. Comparison between nominal composition of the feedstock powder and effective one evaluated on the feedstock and on LPBF-manufactured samples (average ± uncertainty).

wt.%	C	Cr	Ni	Mo	Al	Ti	Fe
Feedstock powder (nominal)	<0.02	12.20	10.00	1.00	0.60	1.00	Bal.
Feedstock powder (ICP-OES)	-	12.5 ± 0.6	10.2 ± 0.8	1.1 ± 0.1	0.5 ± 0.1	1.2 ± 0.3	Bal.
LPBF samples (GD-OES)	0.01 ± 0.005	12.3 ± 0.2	9.8 ± 0.6	1.2 ± 0.1	0.8 ± 0.2	1.1 ± 0.1	Bal.

(**a**)   (**b**)

Figure 1. SEM morphology of particles composing the AMPO M789 feedstock powder at lower (**a**) and higher (**b**) magnification.

Microstructural analyses were performed using a Reichert-Jung MeF3 (Reichert Instruments GmbH, Seefeld, Germany) light optical microscope (LOM) and a Tescan Mira 3 (TESCAN ORSAY Holding, Brno, Czech Republic) field emission scanning electron microscope (SEM) equipped with energy dispersive spectroscopy (EDS) and electron backscattered diffraction (EBSD) by Bruker (Bruker Nano GmbH, Berlin, Germany). Samples for microstructural analyses were hot-mounted in conductive resin, ground up with P1200 grit SiC abrasive paper, and polished with 9 μm, 3 μm, and 1 μm diamond suspensions. Samples were chemically etched for LOM analyses and electrochemically etched with 10% ammonium persulfate in water at 15 V for SEM analyses. Samples for SEM-EBSD underwent a final polishing step with colloidal silica after 1 μm diamond suspension and not etched. X-ray diffraction (XRD) patterns were acquired in the 2θ range at 40–100° using a Philips Empyrean X-ray diffractometer (Malvern Panalytical Ltd., Malvern, UK) equipped with a Cu-K$_\alpha$ source (0.15406 nm). Phase analysis was performed on the acquired

patterns using Panalytical X'Pert HighScore Plus v. 2.2.0 software (Malvern Panalytical Ltd., Malvern, UK) and the ICDD database. The γ-austenite (031-0619 PDF card number) content was evaluated from XRD patterns according to the method defined in ASTM E975-3, based on the integrated intensity of austenite and ferrite/martensite diffraction peaks. Thermodynamic equilibrium calculations were performed using the Thermo-Calc software with the TCFE12 database (Thermo-Calc Software AB, Solna, Sweden).

The ø 13 × 4 mm^2 samples in AB and S conditions underwent isothermal aging treatment in the 470–590 °C temperature range for durations of between 15 min and 16 h in a Nabertherm LT9/14 laboratory furnace (Nabertherm GmbH, Lilienthal, Germany), followed by air cooling. The evolution of hardness was evaluated by Vickers hardness (HV) measurements, performed using a Galileo A200 hardness tester (Officine Galileo, Firenze, Italy) with a 30 kg load and 15 s dwell time.

Differential scanning calorimetry (DSC) and dilatometric tests were performed in the 20–800 °C range to investigate the phase transformations occurring upon heating. DSC tests were performed using a Netzsch 404 F3 Pegasus (Netzsch-Gerätebau GmbH, Selb, Germany) under Ar protective gas at a 20 K/min heating rate. Dilatometric analyses were performed at the same heating rate using a Bähr 805A quench dilatometer (BÄHR-Thermoanalyse GmbH, Hüllhorst, Germany) on the ø 4 × 10 mm samples after polishing with emery papers. Tests were carried out under vacuum (10^{-4} mbar) to prevent oxidation.

3. Results

The LOM, SEM-BSE, and SEM-EBSD micrographs in Figures 2 and 3 show the microstructure of the LPBF M789 steel in the AB and S conditions prior to the aging/over-aging tests. As reported in the literature [25–28], M789 steel possesses, in the AB condition, the typical microstructure of LPBF-manufactured PH-SS of similar composition, composed of melt pool and scan track boundaries at low magnification (Figure 2a), a martensite structure preferentially oriented along the maximum thermal gradient direction during LPBF solidification (i.e., normal to melt pool boundaries, Figures 2a and 3c), and a cellular solidification substructure with sub-μm-sized cells (Figure 2c). Inverse pole figures (IPF) and IPF maps along the building direction (Figure 3a,c) indicate a weak [1 1 1] texture along the vertical building direction, resulting from the LPBF solidification path and following solid-state transformation upon cooling down to room temperature [23,26,30,43]. Despite the exact distribution of alloying elements in the cellular solidification structure not being resolvable through SEM-EDS due to its fine scale, the atomic-number contrast of SEM-BSE imaging (Figure 2c) suggests a higher concentration of heavy alloying elements at the cell boundary, although it is known that the segregation of alloying elements during solidification is determined by the alloy phase diagram (partition coefficient K) and not directly related to the element atomic number. Considering the steel composition (Table 1), it is likely that a higher content of Mo and/or Ni (both possessing a higher atomic number than Fe and thus leading to a brighter SEM-BSE appearance) existed at the cell borders than the cell cores. A similar alloying micro-segregation between cell cores and borders was reported in [17,45,46] for LPBF manufactured maraging steels and in [47] for LPBF manufactured AISI 316L stainless steel. On the other hand, specimens solution annealed at 925 °C and quenched (S) exhibited a homogeneous, not-oriented martensite microstructure with no trace of melt pool boundaries, oriented grains, or a cellular solidification sub-structure (Figure 2b,d and Figure 3b,d). In fact, solution annealing induces alloying diffusion and the transformation of martensite in austenite with a subsequent recrystallization, thus removing the cellular substructure and leading to the nucleation of equiaxed prior austenite grains of homogeneous composition, from which a non-oriented martensite microstructure forms upon rapid cooling [19,21–23,25–28]. XRD analyses (Figure 4) indicated a very low γ-austenite content in not-aged samples, which was slightly higher for AB (2.95 vol.%) than for S (1.94 vol.%). For comparison, a 4.35 vol.% of γ-austenite was measured in the feedstock powder (not reported in Figure 4b). The austenite in not-aged samples can be indicated as retained since it represents a fraction of the parent austenite phase, from

which martensite is formed, and is retained upon rapid cooling. Hardness measurements indicated a hardness of 309 ± 3 HV for S specimens, in line with the typical hardness of conventional PH-SS in the solution-annealed condition prior to aging. A slightly higher hardness (321 ± 5 HV) was measured for AB specimens. In both conditions, the relatively low hardness came from the lack of strengthening intermetallic precipitates, which were formed only during the subsequent aging. In fact, the cooling rate experienced during LPBF process (for AB condition) and water quenching (for S condition) were sufficiently high to prevent the precipitation of secondary intermetallic phases (such as strengthening precipitates), thus resulting in high alloying supersaturation being retained in the resulting martensite microstructure [48]. Previous works [19,49] indicated dislocations and grain boundary strengthening as the main strengthening mechanisms operating in LPBF-manufactured PH-SS in the AB condition. Therefore, the slightly higher hardness in the AB condition compared to the S one, despite the higher austenite content, might indicate a higher dislocation and grain boundary contribution to strengthening, possibly related to the different microstructures resulting from the LPBF process (for AB specimens) and from solution annealing and quenching (for the S condition).
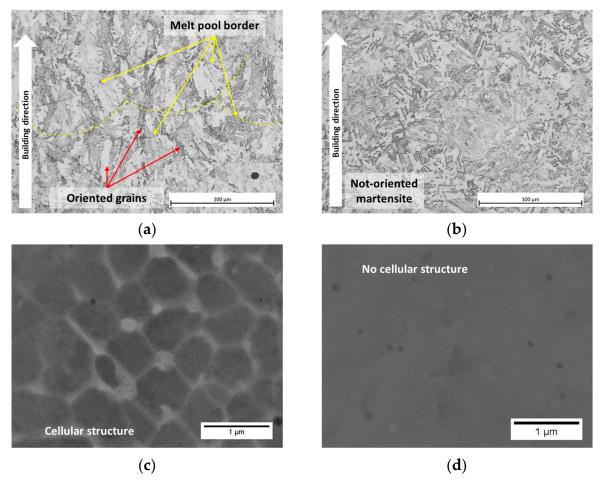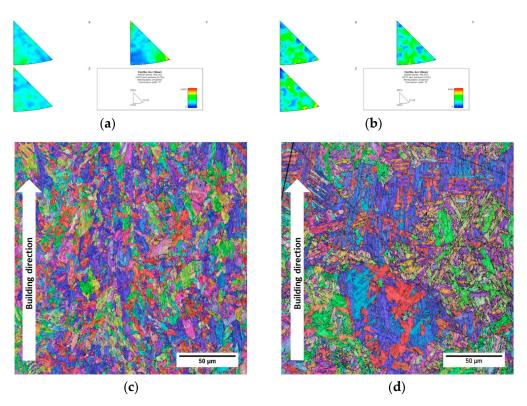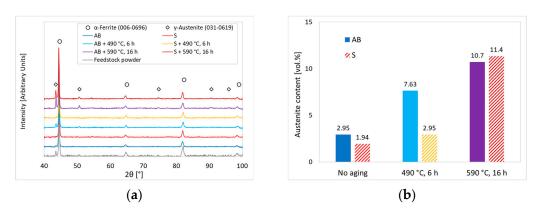

Figure 2. LOM (**a**,**b**) and SEM-BSE (**c**,**d**) microstructure of samples in the AB (**a**,**c**) and S (**b**,**d**) conditions. Yellow arrows and dashed lines highlight melt pool borders, whereas red arrows point out oriented grains.

Figure 3. Results of SEM-EBSD analyses on AB (**a**,**c**) and S (**b**,**d**) samples: inverse pole figures (**a**,**b**) and inverse pole figure maps along the vertical direction (**c**,**d**).
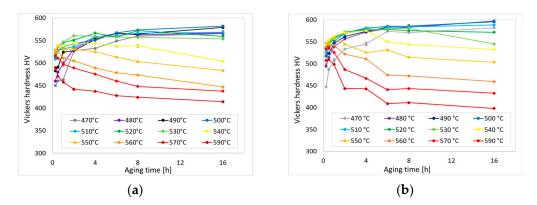

Figure 4. XRD patterns acquired from the feedstock powder and from AB and S specimens aged in different conditions (no aging, 490 °C for 6 h, 590 °C for 16 h) (**a**) and volume fraction of austenite calculated according to ASTM E975-3 (**b**).

The aging curves in Figure 5 show the trend of hardness as a function of temperature and time for the AB and S samples. For both conditions, two distinct behaviours can be identified:

i. Hardening at the lower aging temperatures (below 530 °C), at which point hardness monotonically increased with increasing aging duration;

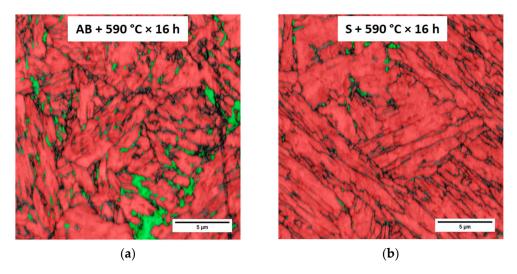ii. Softening (above 530 °C), where hardness decreased with both increasing aging temperature and time.

Figure 5. Aging curves for AB (**a**) and S (**b**) specimens.

Both the AB and S samples reached a comparable peak hardness in the range of 580–600 HV for aging temperatures between 480 and 510 °C and a similar minimum hardness value of approximatively 400 HV after 16 h at 590 °C.
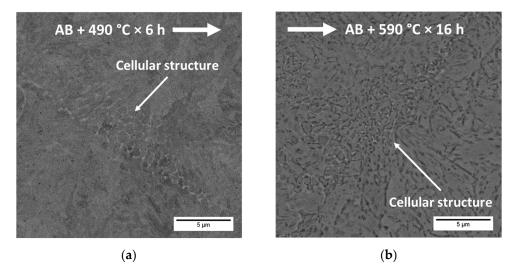
XRD analyses on peak-aged (490 °C for 6 h) samples (Figure 4) indicated that in the S samples the austenite content did not vary significantly with respect to the not-aged ones. On the other hand, it roughly doubled in the AB samples, from 2.95% prior to aging to ~7.6% after peak aging. After over-aging at 590 °C for 16 h, a significantly higher austenite content was measured in both the AB and S samples, at around 11 vol.% for both heat treatment conditions. Noticeably, samples over-aged at 590 °C for 16 h also exhibited the minimum hardness (Figure 5). The austenite formed during aging in PH-SS and maraging steels is usually referred to as reverted austenite, since it comes from the reversion of α'-martensite in γ-austenite at temperatures approaching the austenite phase stability field [1,2,50–52]. The relevant content of reverted austenite in over-aged specimens can account, at least to some extent, for the low hardness. However, the comparison between peak-aged (490 °C for 6 h) and over-aged (590 °C for 16 h) conditions shows that, in the investigated range of over-aging temperatures and durations, hardness decreased by ~30%, whereas the increase in austenite content was below 10%. SEM-EBSD phase maps (Figure 6) show that austenite reversion in over-aged samples preferentially occurred at the sub-grain boundaries of the martensite structure (at inter-lath, packet, and block boundaries). Moreover, austenite reversion in AB specimens also occurred at the cellular substructure. SEM-BSE images in Figure 7 clearly show that the cellular structure in AB specimens was retained after aging at peak hardening (490 °C for 6 h, Figure 7a) and over-aging at 590 °C for 16 h (Figure 7b), suggesting that higher temperatures are required to homogenise the alloying distribution and thus remove the micro-segregation.

Equilibrium thermodynamic calculations (Figure 8) predicted that several intermetallic compounds would be stable in the temperature range investigated during the aging/over-aging tests. In particular, $Ni_3(Ti,Al)$ was predicted to be stable up to 533 °C, with a solvus temperature of 565 °C. Between 533 and 565 °C, the gradual dissolution of $Ni_3(Ti,Al)$ was paired with the formation of Ni_3Ti. As it is clarified in Section 4, $Ni_3(Ti,Al)$ and Ni_3Ti were expected to demonstrate distinct crystal structure and properties, despite the similar composition and stoichiometry. Above 621 °C (not investigated during aging/over-aging tests), only the $Fe_2(Mo,Ti)$ intermetallic phase was predicted. Considering $\alpha' \rightarrow \gamma$ reversion, the calculations indicated austenite starting (A_s) and finishing (A_f) transformation temperatures of 533 °C and 696 °C, respectively. Noticeably, the predicted temperatures at which austenite reversion and $Ni_3(Ti,Al)$ dissolution initiate corresponded, according to the thermodynamic calculations.

Figure 6. SEM-EBSD phase maps showing the distribution of α'-martensite (in red) and reverted γ-austenite (in green) in AB (**a**) and S (**b**) samples over-aged at 590 °C for 16 h.

Figure 7. SEM-BSE micrographs of AB specimens aged at 490 °C for 6 h (**a**) and 590 °C for 16 h (**b**) showing the persistence of the cellular structure.
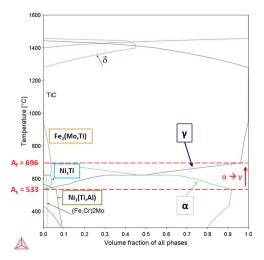

Figure 8. Equilibrium phases predicted by thermodynamic calculations.

Figure 9a,b show DSC and dilatometric (first-derivative of strain vs. temperature) curves, respectively, obtained at a heating rate of 20 K/min. The different appearance between the AB and S curves in Figure 9,b is due to the different scale. Two main peaks marked with the Roman numerals "I" and "II" were identified in the temperature ranges of 400–550 °C and 550–700 °C, respectively. Peak I (strong exothermic signal on DSC curves, contraction on first-derivative dilatometric curves) was likely to be associated with the precipitation of strengthening $Ni_3(Ti,Al)$ and thus with the hardening observed for $T \leq 530$ °C. On the other hand, peak II (contraction on dilatometric curves) was attributed to the $\alpha' \rightarrow \gamma$ reversion occurring at higher temperatures, at which aging and over-aging tests indicated softening. The onset temperature for peak II from dilatometric analyses (~530 °C) roughly matched the equilibrium A_s temperature predicted from the thermodynamic calculations (Figure 8). Instead, the endset temperature of peak II appeared to be slightly higher than the predicted A_f. The identification of peak II from DSC curves was not straightforward, possibly due to the superposition of several transformations. Within the temperature range corresponding to peak II, DSC distinctly revealed a minor exothermic peak in the range of 570–650 °C (indicated as "X" in Figure 9b), visible also in the first-derivative dilatometric curve for the AB specimen. According to the existing literature, several microstructural transformations might occur and superpose in the temperature range corresponding to peak II, the main one of which is $\alpha' \rightarrow \gamma$ reversion, which is also accompanied by a change in specific heat (slope of DSC curve baseline) and the coefficient of thermal expansion (slope of the strain vs. temperature dilatometric curve, not visible from the first-derivative curves in Figure 9a) [53–55]. The thermodynamic calculations in Figure 8 predicted the possible precipitation and dissolution of other intermetallic compounds besides $Ni_3(Ti,Al)$ starting from 533 °C, which might possibly superimpose to the $\alpha' \rightarrow \gamma$ reversion, thus further complicating the interpretation of DSC and dilatometric curves. Another possibly involved transformation is the ferromagnetic-to-paramagnetic transition at the Curie temperature T_C, which, however, should appear as a contraction on dilatometric curves [56]. Therefore, the variety of possible microstructural changes occurring within the temperature range corresponding to peak II does not enable the complete identification of all the observed peaks.
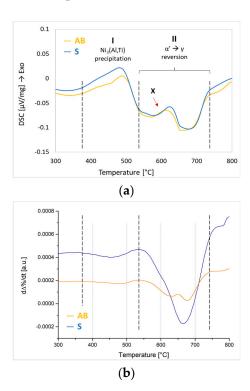

(**a**)

(**b**)

Figure 9. Results of DSC (**a**) and dilatometric (**b**) analyses.

4. Discussion

As described in the Introduction section, hardening in PH-SS and maraging steels (and in general in precipitation-strengthened alloys) is associated with the precipitation of extremely fine intermetallic particles, which hinder the motion of dislocations by different mechanisms based on their characteristics and interaction with the surrounding matrix [3]. The strengthening compound precipitating during aging depends on the specific alloy system. For example, copper-bearing PH-SS (such as 17–4 PH and 15–5 PH) are reinforced by ε-Cu particles with a face-centred cubic (fcc) crystal structure [1,5]. PH-SS containing Ni and Al, such as PH 13–8 Mo, CX, and Corrax steels, are strengthened by β-NiAl with a CsCl structure, whereas superior-strength grades also containing Ti are hardened by γ'-Ni_3(Ti,Al) with an $L1_2$ fcc structure and/or η-Ni_3Ti with a $D0_{24}$ hexagonal structure, depending on the Ti/Al ratio [4,57,58]. The higher hardness and strength of maraging steels come from orthorhombic Ni_3Mo and η-Ni_3Ti precipitates [6,59]. According to Riabov et al. [57], γ'-Ni_3X is the major hardener in steels with a composition close to the one investigated in the present work, where X represents one or more elements among Al, Ti, Si, Mn, and Nb. Tian et al. [26] indicated Ni_3(Ti,Al) as the main strengthening phase in the same steel investigated in the present work (AMPO M789). In contrast to γ' phase, η-Ni_3Ti has no solubility for other elements beside Ti and has a different crystal structure. The aging curves in Figure 5 show that there was an extremely rapid hardness increase in the early stages of aging, i.e., within the first 15 min at temperatures above 490–500 °C, reaching values exceeding 80% of the peak hardness (from ~50% in the AB and S conditions). According to [6], the rapid hardening of PH-SS and maraging steels is indicative of the absence of a free-energy barrier for precipitation, resulting from a low precipitate–matrix lattice mismatch, high solute supersaturation (i.e., large driving force for precipitation), and high dislocation density of the martensite microstructure, which represent favourable nuclei for precipitation. Depending on the alloy system and precipitating phase, precipitates can nucleate homogeneously via the formation of solute-rich clusters or heterogeneously on dislocations [58]. Although the type, stoichiometry, crystal structure, and formation mechanism of precipitates depend on the specific alloy system, the strengthening effect is proportional to the precipitates distribution in terms of size, volume density, and number fraction, and therefore an optimal distribution exists that leads to peak hardening. On the other hand, for excessive aging temperature and duration (over-aging), larger particles grow at the expense of finer ones, which are redissolved in the matrix following so-called Ostwald ripening [3]. Over-aging leads to a not-optimal distribution of coarse precipitates with a low number density, causing softening. Riabov et al. [57] demonstrated an extremely low coarsening rate for γ'-Ni_3X precipitates, with an average radius of only 2 nm after 18 h of aging at 500 °C. γ'-Ni_3(Al,Ti) is indeed the main strengthening phase in Ni-based superalloys and in austenitic PH-SS A286, specifically designed for high-temperature applications [4]. The coarsening kinetic of strengthening precipitates is well described by the Lifshitz–Slyozov–Wagner (LSW) model, which relates particle size to aging/over-aging temperature and time:

$$\overline{r(t)}^3 - \overline{r_0}^3 = K \cdot t \tag{1}$$

where $\overline{r_0}$ and $\overline{r(t)}$ are the mean precipitate radius at the beginning of aging and at the aging time t, respectively, and K is the coarsening rate. Precipitate growth is a diffusion-controlled process in which the rate-limiting factor is the diffusion of solute atoms through the matrix lattice, so the coarsening rate K can be expressed in the form:

$$K = A \cdot \frac{1}{T} \cdot e^{-\frac{Q}{RT}} \tag{2}$$

in which the constant A depends on the precipitate–matrix interfacial energy, solute concentration at equilibrium, atomic volume, and diffusion coefficient. T indicates the absolute aging temperature, R the universal gas constant, and Q the activation energy for the in-

volved diffusion process. In fact, the Arrhenius-type exponential term in Equation (2) comes from the dependence of the diffusivity D on temperature:

$$D = D_0 \cdot e^{-\frac{Q}{RT}} \tag{3}$$

where D_0 is a diffusion coefficient (embedded in parameter A in Equation (2)). The LSW model can be used to describe the evolution of the hardness during both aging and over-aging (thus, hardening and softening) only if precipitate growth and coarsening is the only underlying microstructural change involved. This is generally verified for age-hardenable aluminium alloys and γ'-strengthened Ni-based superalloys [3]. However, α'-martensite-to-γ-austenite reversion plays a relevant role in the over-aging of martensitic PH-SS and maraging steels [1,2,6,50–52,60–62]. In fact, increasing fractions of reverted austenite lead to lower hardness and strength but higher ductility and toughness. For this reason, in the heat treatment of martensitic PH-SS it is possible to achieve desired combinations of strength and toughness apart from peak hardening by controlling the amount of reverted austenite, hence deliberately over-aging the steel by adjusting the aging temperature and time [1,4]. However, it must be considered that reverted austenite is metastable at room temperature and can transform back to martensite under applied stresses, further affecting the mechanical response of the alloy as well as the dimensional stability of the final part [51].

In order to separate the contribution of precipitate coarsening and austenite reversion during the aging and over-aging of the investigated steel, master curves of hardness were computed from aging curves (Figure 10) by plotting hardness as a function of the so-called Larson–Miller Parameter:

$$LMP = T \cdot (C + \log_{10} t) \tag{4}$$

where C is an empirical best-fit constant depending on the rate-limiting diffusive process, T is the absolute aging temperature (in K), and t is the aging time (in hours). LMP can be exploited to describe the cumulative effect of temperature and time on diffusion-controlled processes, such as creep, residual stress relief, microstructure recovery, and recrystallisation [63,64]. The low scatter of the LMP-HV master curves in Figure 10 indicates the effectiveness of LMP at describing the hardening and softening of the considered steel. Noticeably, closely similar curves were obtained for the AB and S conditions, confirming the absence of significant differences between the two heat treatment conditions in terms of aging and over-aging responses despite the different microstructure. However, it was not possible to obtain a single master curve comprising both aging and over-aging; instead, two separate curves for hardening (T ≤ 530 °C) and softening (T > 530 °C) due to the different values for the best-fit parameter (C = 15 for T ≤ 530, C = 42 for T > 530 °C) were obtained. According to [64], the value of C is strictly related to the activation energy Q of the underlying rate-limiting diffusive process, so a large transition of C can be considered to be indicative of different transformations involved in hardening and softening. The apparent energy Q_{App} for hardening (T ≤ 530 °C), calculated from the hardness curves following the method described in [65], was equal to 245 kJ/mol for the S samples (R^2 = 0.96) and 253 kJ/mol for the AB ones (R^2 = 0.91) and thus was extremely close to the activation energy for Ni diffusion in the ferromagnetic α-ferrite lattice (246 kJ/mol [66]). As reported by [51], this further supports that hardening at low aging temperatures occurs via precipitation of Ni-rich strengthening compounds, presumably γ'-Ni$_3$(Al,Ti), considering the thermodynamic calculations in Figure 8 and previous studies [26,57]. On the opposite, the apparent energy for softening was calculated as 423 kJ/mol for S (R^2 = 0.93) and 544 kJ/mol for AB samples (R^2 = 0.99), and hence was considerably higher than for hardening, further supporting the involvement of a different transformation apart from precipitate coarsening in the over-aging of the considered PH-SS, possibly austenite reversion. Values reported in the literature for the activation energy for austenite reversion in PH 13–8 Mo PH-SS and maraging steels are in the range of 234–421 kJ/mol [50,51,60,61] depending on the steel chemistry. Moreover, an interaction between $\alpha' \rightarrow \gamma$ reversion and the precipitation, coarsening, and dissolution of precipitates during over-aging is
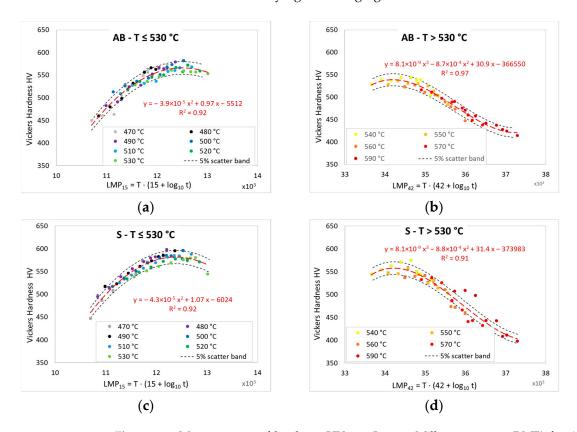
reported for PH 13–8 Mo and maraging steels [6,50–52,59,62]. Schnitzer et al. [51] proposed a model describing the interrelation between austenite reversion and precipitation and dissolution of the strengthening β-NiAl intermetallic in PH 13–8 Mo based on experimental measurements and thermodynamic calculations. According to Schnitzer et al., both β-NiAl and austenite reversion are thermodynamically possible from virgin martensite and thus could theoretically proceed independently of each other during the first stages of aging. For increasing aging temperature, a higher fraction of α'-martensite is reverted to γ-austenite, as also predicted by the thermodynamic calculations shown in Figure 8. At the same time, strengthening precipitates coarsen and are redissolved, releasing Ni and Al in the surrounding matrix. Although Al preferentially diffuses towards the remaining, larger precipitates, contributing to further coarsening (Ostwald ripening), Ni promotes the reversion of increasing fractions of α'-martensite into γ-austenite. According to Schnitzer et al., the reverted γ-austenite is free from β-NiAl precipitates. Sha et al. [59] reported that, in maraging steels, the precipitation of Ni-rich Ni_3X phases anticipates austenite reversion during the early stages of aging due to kinetics. The extensive precipitation of Ni-rich strengthening phases consumes large amounts of Ni, depleting the α' matrix and thus increasing the A_s temperature with respect to a precipitate-free matrix. The dissolution of these precipitates during over-aging at higher temperatures re-distributes Ni in the α' matrix, thus decreasing A_s and promoting α' → γ reversion. Moreover, it is reported that the dissolution of Ni_3Ti and Ni_3Mo precipitates during the over-aging of maraging steels is concomitant with the precipitation of Fe-rich Fe_2Mo laves and/or μ-Fe_7Mo_6 intermetallic phases, which depletes the α'-matrix of Fe, thus further decreasing A_s by increasing the relative concentration of Ni [59,67]. To the authors' knowledge, the formation of Fe-rich, Ni-free intermetallic phases (Fe_2Mo, Fe_7Mo_6, etc.) is not reported in the literature for PH 13–8 Mo and PH-SS with similar compositions. However, for the M789 steel investigated in the present work, thermodynamic calculations in Figure 8 predicted the formation of $Fe_2(Mo,Ti)$ at 621 °C together with the dissolution of Ni_3Ti. Therefore, it is possible that the precipitation and dissolution of additional intermetallic phases beside Ni-rich ones occurred during the aging and over-aging of the M789 steel, possibly contributing to austenite reversion and softening. However, this hypothesis requires further and more detailed microstructural investigations to be confirmed.

Considering the effect of the different microstructure, the aging (Figure 5) and master curves (Figure 10) did not show substantial differences between the AB and solution-annealed (S) samples in terms of aging response. Therefore, it can be inferred that the precipitation reaction responsible for hardening is not affected by the different microstructure—i.e., the presence of the LPBF structure featuring a cellular solidification substructure, an oriented martensite, and melt pool/scan track boundaries has no appreciable effect on the precipitation of strengthening $Ni_3(Al,Ti)$ phases, as further confirmed by the similar apparent energy Q_{App}. Concerning over-aging, Q_{App} for softening appeared to be significantly higher for AB specimens than for S ones, possibly suggesting a higher resistance to softening. However, Figures 5 and 10 clearly indicate an equivalent softening behaviour between the two heat treatment conditions. Therefore, it is possible that the calculation of Q_{App} for softening could be affected by the higher variability of aging curves in the S condition, as visible from the master curve in Figure 10d. The higher content of austenite in peak-hardening conditions (490 °C for 6 h) for AB samples (7.6%) than for S ones (2.95%), indicating a higher α' → γ reversion at early stages of aging, is likely to be attributable to the different microstructure and, in particular, to the cellular solidification substructure present in the AB condition and eliminated by the solution annealing (Figure 2). The atomic number contrast of SEM-BSE imaging suggests the segregation of elements with high atomic numbers (Mo, Ni, . . .) at the boundaries of the cellular substructure, which could promote austenite reversion at low temperatures. However, no difference in terms of reverted austenite was observed between AB and S specimens over-aged at the highest temperature and duration (590 °C for 16 h, above the predicted A_s) and exhibiting the lowest hardness (~400 HV), although Figure 7 indicates the retention of the cellular substructure in the

AB samples. Therefore, the cellular solidification structure appears to have been effective in promoting austenite reversion only at the lowest aging temperatures, around peak-hardening conditions, at which no or very limited reversion occurs for a microstructure with homogeneous composition (S samples). However, this effect became negligible at higher temperatures (belonging to the over-aging regime) and, in particular, above A_s, at which point $\alpha' \rightarrow \gamma$ reversion is thermodynamically expected also for a homogeneous microstructure with no alloying micro-segregation.
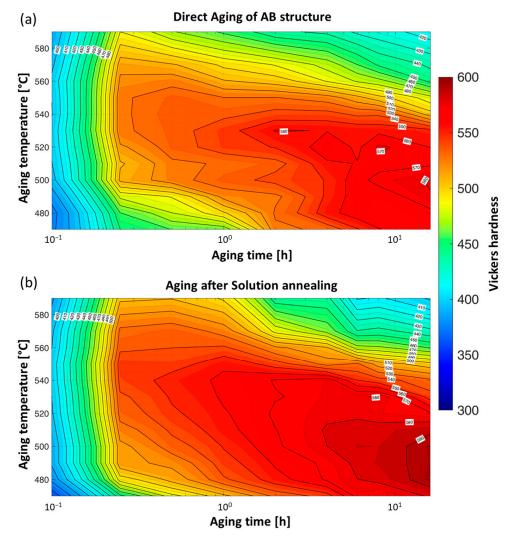

Figure 10. Master curves of hardness HV vs. Larson–Miller parameter (LMP) for AB (**a**,**b**) and S (**c**,**d**) samples. Note the different C values between hardening (**a**,**c**) and softening (**b**,**d**) master curves.

In view of a practical application of LPBF-manufactured M789 steel for the production of dies for plastic injection moulding, the following basic guidelines can be drawn to aid the heat treatment procedure selection between direct aging (DA) of the AB structure and the aging of solution-annealed and -quenched samples, i.e., solution annealing and aging (SA):

- One-step, low-temperature DA enables a great simplification of the heat treatment procedure and a resulting reduction in time, energy consumption, and cost due to the elimination of the high-temperature step of solution annealing and quenching.
- The aging and over-aging behaviour of the M789 steel is comparable between the AB and S conditions and thus is not substantially affected by the solution annealing. A similar maximum hardness (580–600 HV) can be achieved in peak-aging condition (490 °C, 6 h)
- Proper aging parameters can be selected by using iso-hardness maps (contour plot of hardness as a function of aging temperature and time) such as the ones in Figure 11, obtained from the hardness curves in Figure 5.
- Solution annealing results in a more homogeneous and isotropic martensite microstructure compared to the LPBF AB condition. Upon aging at low temperature (around peak-hardening), the homogeneous microstructure of S specimens leads to lower

fraction of reverted austenite. At high temperature (over-aging), no difference seems to exist in terms of austenite reversion between the AB and S samples.

- Although no significant difference exists between the AB and S specimens in terms of aging response, peak hardness, and softening upon over-aging despite the significantly different microstructures, it is possible that a difference between the AB and S conditions exists in terms of mechanical behaviour involving (i) anisotropy, associated with the hierarchical and anisotropic structure of the AB condition absent in the S one, and (ii) dimensional stability under applied loads, related to the higher content of metastable retained austenite for AB specimens at peak aging [68]. Therefore, dedicated mechanical tests are required to investigate the suitability of the two conditions.

Figure 11. Iso-hardness maps showing the combined effect of aging/over-aging temperature and time on the hardness of AB (**a**) and S (**b**) samples.

5. Conclusions

In the present work, the aging and over-aging behaviour of a 12.2Cr-10Ni-1Mo-1Ti-0.6Al PH-SS (AMPO M789) manufactured via LPBF was investigated in terms of microstructure, including austenite content and hardness, in order to assess its feasibility for applications involving prolonged service at high temperature—for example, in dies for plastic injection moulding. The effect of a different microstructure, resulting from the application or not of a solution-annealing heat treatment before aging, was investigated. The following remarks can be drawn:

- In the as-built (AB) condition, the steel exhibited the typical hierarchical structure of LPBF-manufactured parts. The application of a solution-annealing treatment eliminated the LPBF AB structure, resulting in a homogeneous, isotropic, martensite microstructure.
- AB and solution-annealed (S) specimens exhibited the same aging and over-aging behaviour, despite the different microstructure.
- Hardening during aging was associated with the precipitation of Ni-rich particles, whereas softening upon over-aging at higher temperature involved both precipitates coarsening and martensite-to-austenite reversion.
- The cellular solidification structure of LPBF AB samples promoted austenite reversion at low aging temperature (around peak hardening, 490 °C). On the other hand, no difference between AB and S samples was observed at high temperature, despite the retention of the cellular structure.
- Direct aging (DA) of the LPBF AB structure appears to be a promising procedure to reduce heat treatment cost and duration without impairing the maximum achievable hardness and over-aging behaviour. However, eventual differences in terms of mechanical properties, possibly related to the different microstructure and austenite content in peak-hardening conditions, must be evaluated in order to assess the suitability of one heat treatment procedure over another for the specific application.

Author Contributions: Conceptualisation, A.M., M.Z. and M.P.; methodology, M.Z. and M.P.; investigation, M.Z. and M.P.; data curation, M.Z. and M.P.; writing—original draft preparation, A.M., M.Z. and M.P.; writing—review and editing, A.M., M.Z., A.F., L.C. and M.P.; supervision, A.F., L.C. and M.P.; funding acquisition, A.F., A.M. and L.C. All authors have read and agreed to the published version of the manuscript.

Data Availability Statement: The data required to reproduce the findings reported in the present work are available in the diagrams, tables, and images of this manuscript.

Conflicts of Interest: The authors declare no conflict of interest.

References

1. McGuire, M.F. *Stainless Steels for Design Engineers*; ASM International: Materials Park, OH, USA, 2008; ISBN 978-1-62708-286-0.
2. Pollard, B. Selection of Wrought Precipitation-Hardening Stainless Steels. In *Welding, Brazing, and Soldering*; ASM International: Materials Park, OH, USA, 1993; pp. 482–494.
3. Smallman, R.E.; Ngan, A.H.W. Precipitation Hardening. In *Modern Physical Metallurgy*; Elsevier: Amsterdam, The Netherlands, 2014; pp. 499–527.
4. Li, L. Heat Treating of Precipitation-Hardenable Stainless Steels and Iron-Base Superalloys. In *Heat Treating of Irons and Steels*; ASM International: Materials Park, OH, USA, 2014; pp. 397–417.
5. Prakash Kolli, R.; Seidman, D.N. Heat Treatment of Copper Precipitation-Strengthened Steels. In *Heat Treating of Irons and Steels*; ASM International: Materials Park, OH, USA, 2014; pp. 188–203.
6. Carson, C. Heat Treating of Maraging Steels. In *Heat Treating of Irons and Steels*; ASM International: Materials Park, OH, USA, 2014; pp. 468–480.
7. Kaufman, J.G. *Introduction to Aluminium Alloys and Tempers*; ASM International: Materials Park, OH, USA, 2000; ISBN 978-0-87170-689-8.
8. DebRoy, T.; Wei, H.L.; Zuback, J.S.; Mukherjee, T.; Elmer, J.W.; Milewski, J.O.; Beese, A.M.; Wilson-Heid, A.; De, A.; Zhang, W. Additive Manufacturing of Metallic Components—Process, Structure and Properties. *Prog. Mater. Sci.* **2018**, *92*, 112–224. [CrossRef]
9. Yap, C.Y.; Chua, C.K.; Dong, Z.L.; Liu, Z.H.; Zhang, D.Q.; Loh, L.E.; Sing, S.L. Review of Selective Laser Melting: Materials and Applications. *Appl. Phys. Rev.* **2015**, *2*, 041101. [CrossRef]
10. Hebert, R.J. Viewpoint: Metallurgical Aspects of Powder Bed Metal Additive Manufacturing. *J. Mater. Sci.* **2016**, *51*, 1165–1175. [CrossRef]
11. Herzog, D.; Seyda, V.; Wycisk, E.; Emmelmann, C. Additive Manufacturing of Metals. *Acta Mater.* **2016**, *117*, 371–392. [CrossRef]

12. Nandwana, P. Additive Manufacturing of Tool Steels. In *Additive Manufacturing Processes*; ASM International: Materials Park, OH, USA, 2020; pp. 366–373.

13. Vafadar, A.; Guzzomi, F.; Rassau, A.; Hayward, K. Advances in Metal Additive Manufacturing: A Review of Common Processes, Industrial Applications, and Current Challenges. *Appl. Sci.* **2021**, *11*, 1213. [CrossRef]

14. Asgari, H.; Mohammadi, M. Microstructure and Mechanical Properties of Stainless Steel CX Manufactured by Direct Metal Laser Sintering. *Mater. Sci. Eng. A* **2018**, *709*, 82–89. [CrossRef]

15. Turk, C.; Zunko, H.; Aumayr, C.; Leitner, H.; Kapp, M. Advances in Maraging Steels for Additive Manufacturing. *BHM Berg- und Hüttenmännische Monatshefte* **2019**, *164*, 112–116. [CrossRef]

16. Zitelli, C.; Folgarait, P.; Di Schino, A. Laser Powder Bed Fusion of Stainless Steel Grades: A Review. *Metals* **2019**, *9*, 731. [CrossRef]

17. Bajaj, P.; Hariharan, A.; Kini, A.; Kürnsteiner, P.; Raabe, D.; Jägle, E.A. Steels in Additive Manufacturing: A Review of Their Microstructure and Properties. *Mater. Sci. Eng. A* **2020**, *772*, 138633. [CrossRef]

18. Zai, L.; Zhang, C.; Wang, Y.; Guo, W.; Wellmann, D.; Tong, X.; Tian, Y. Laser Powder Bed Fusion of Precipitation-Hardened Martensitic Stainless Steels: A Review. *Metals* **2020**, *10*, 255. [CrossRef]

19. Hadadzadeh, A.; Shahriari, A.; Amirkhiz, B.S.; Li, J.; Mohammadi, M. Additive Manufacturing of an Fe–Cr–Ni–Al Maraging Stainless Steel: Microstructure Evolution, Heat Treatment, and Strengthening Mechanisms. *Mater. Sci. Eng. A* **2020**, *787*, 139470. [CrossRef]

20. Shahriari, A.; Khaksar, L.; Nasiri, A.; Hadadzadeh, A.; Amirkhiz, B.S.; Mohammadi, M. Microstructure and Corrosion Behavior of a Novel Additively Manufactured Maraging Stainless Steel. *Electrochim. Acta* **2020**, *339*, 135925. [CrossRef]

21. Li, K.; Zhan, J.; Yang, T.; To, A.C.; Tan, S.; Tang, Q.; Cao, H.; Murr, L.E. Homogenization Timing Effect on Microstructure and Precipitation Strengthening of 17–4PH Stainless Steel Fabricated by Laser Powder Bed Fusion. *Addit. Manuf.* **2022**, *52*, 102672. [CrossRef]

22. Zhang, J.; Wang, M.; Niu, L.; Liu, J.; Wang, J.; Liu, Y.; Shi, Z. Effect of Process Parameters and Heat Treatment on the Properties of Stainless Steel CX Fabricated by Selective Laser Melting. *J. Alloys Compd.* **2021**, *877*, 160062. [CrossRef]

23. Afkhami, S.; Javaheri, V.; Dabiri, E.; Piili, H.; Björk, T. Effects of Manufacturing Parameters, Heat Treatment, and Machining on the Physical and Mechanical Properties of 13Cr10Ni1·7Mo2Al0·4Mn0·4Si Steel Processed by Laser Powder Bed Fusion. *Mater. Sci. Eng. A* **2022**, *832*, 142402. [CrossRef]

24. Chadha, K.; Tian, Y.; Jiang, L.; Dorin, T.; Spray, J.; Aranas, C. Strengthening Mechanisms in a New Precipitation Hardening Stainless Steel Fabricated by Laser Powder Bed Fusion. *MRS Commun.* **2022**, *12*, 365–369. [CrossRef]

25. Palad, R.; Tian, Y.; Chadha, K.; Rodrigues, S.; Aranas, C. Microstructural Features of Novel Corrosion-Resistant Maraging Steel Manufactured by Laser Powder Bed Fusion. *Mater. Lett.* **2020**, *275*, 128026. [CrossRef]

26. Tian, Y.; Palad, R.; Aranas, C. Microstructural Evolution and Mechanical Properties of a Newly Designed Steel Fabricated by Laser Powder Bed Fusion. *Addit. Manuf.* **2020**, *36*, 101495. [CrossRef]

27. Tian, Y.; Palad, R.; Jiang, L.; Dorin, T.; Chadha, K.; Aranas, C. The Effect of Heat Treatments on Mechanical Properties of M789 Steel Fabricated by Laser Powder Bed Fusion. *J. Alloys Compd.* **2021**, *885*, 161033. [CrossRef]

28. Brytan, Z.; Król, M.; Benedyk, M.; Pakieła, W.; Tański, T.; Dagnaw, M.J.; Snopiński, P.; Pagáč, M.; Czech, A. Microstructural and Mechanical Properties of Novel Co-Free Maraging Steel M789 Prepared by Additive Manufacturing. *Materials* **2022**, *15*, 1734. [CrossRef] [PubMed]

29. Tian, Y.; Nyamuchiwa, K.; Chadha, K.; He, Y.; Aranas, C. Laser Powder Bed Fusion of M789 Maraging Steel on Cr–Mo N709 Steel: Microstructure, Texture, and Mechanical Properties. *Mater. Sci. Eng. A* **2022**, *839*, 142827. [CrossRef]

30. Haghdadi, N.; Laleh, M.; Moyle, M.; Primig, S. Additive Manufacturing of Steels: A Review of Achievements and Challenges. *J. Mater. Sci.* **2021**, *56*, 64–107. [CrossRef]

31. LeBrun, T.; Nakamoto, T.; Horikawa, K.; Kobayashi, H. Effect of Retained Austenite on Subsequent Thermal Processing and Resultant Mechanical Properties of Selective Laser Melted 17–4 PH Stainless Steel. *Mater. Des.* **2015**, *81*, 44–53. [CrossRef]

32. Cheruvathur, S.; Lass, E.A.; Campbell, C.E. Additive Manufacturing of 17-4 PH Stainless Steel: Post-Processing Heat Treatment to Achieve Uniform Reproducible Microstructure. *JOM* **2016**, *68*, 930–942. [CrossRef]

33. Mahmoudi, M.; Elwany, A.; Yadollahi, A.; Thompson, S.M.; Bian, L.; Shamsaei, N. Mechanical Properties and Microstructural Characterization of Selective Laser Melted 17-4 PH Stainless Steel. *Rapid Prototyp. J.* **2017**, *23*, 280–294. [CrossRef]

34. Burns, D.E.; Kudzal, A.; McWilliams, B.; Manjarres, J.; Hedges, D.; Parker, P.A. Investigating Additively Manufactured 17-4 PH for Structural Applications. *J. Mater. Eng. Perform.* **2019**, *28*, 4943–4951. [CrossRef]

35. Hsu, T.-H.; Chang, Y.-J.; Huang, C.-Y.; Yen, H.-W.; Chen, C.-P.; Jen, K.-K.; Yeh, A.-C. Microstructure and Property of a Selective Laser Melting Process Induced Oxide Dispersion Strengthened 17-4 PH Stainless Steel. *J. Alloys Compd.* **2019**, *803*, 30–41. [CrossRef]

36. Oh, W.J.; Son, Y.; Cho, S.Y.; Yang, S.W.; Shin, G.Y.; Shim, D.S. Solution Annealing and Precipitation Hardening Effect on the Mechanical Properties of 630 Stainless Steel Fabricated via Laser Melting Deposition. *Mater. Sci. Eng. A* **2020**, *794*, 139999. [CrossRef]

37. Lashgari, H.R.; Kong, C.; Adabifiroozjaei, E.; Li, S. Microstructure, Post Thermal Treatment Response, and Tribological Properties of 3D Printed 17-4 PH Stainless Steel. *Wear* **2020**, *456–457*, 203367. [CrossRef]

38. Sarkar, S.; Mukherjee, S.; Kumar, C.S.; Kumar Nath, A. Effects of Heat Treatment on Microstructure, Mechanical and Corrosion Properties of 15-5 PH Stainless Steel Parts Built by Selective Laser Melting Process. *J. Manuf. Process.* **2020**, *50*, 279–294. [CrossRef]

39. Kultz Unti, L.F.; Aota, L.S.; Jardini, A.L.; Tschiptschin, A.P.; Sandim, H.R.Z.; Jägle, E.A.; Zilnyk, K.D. Microstructural Characterization of 15-5PH Stainless Steel Processed by Laser Powder-Bed Fusion. *Mater. Charact.* **2021**, *181*, 111485. [CrossRef]

40. Campbell, C.E.; Stoudt, M.R.; Zhang, F. Additive Manufacturing of Steels and Stainless Steels. In *Additive Manufacturing Processes*; ASM International: Materials Park, OH, USA, 2020; pp. 346–365.

41. Dong, D.; Chang, C.; Wang, H.; Yan, X.; Ma, W.; Liu, M.; Deng, S.; Gardan, J.; Bolot, R.; Liao, H. Selective Laser Melting (SLM) of CX Stainless Steel: Theoretical Calculation, Process Optimization and Strengthening Mechanism. *J. Mater. Sci. Technol.* **2021**, *73*, 151–164. [CrossRef]

42. Turnier Trottier, W.; Kreitcberg, A.; Brailovski, V. Structure and Mechanical Properties of Laser Powder Bed-Fused and Wrought PH13-8Mo-Type Precipitation Hardening Stainless Steels: Comparative Study. *J. Manuf. Mater. Process.* **2021**, *5*, 67. [CrossRef]

43. Wei, S.; Kumar, P.; Lau, K.B.; Wuu, D.; Liew, L.-L.; Wei, F.; Teo, S.L.; Cheong, A.; Ng, C.K.; Zhang, B.; et al. Effect of Heat Treatment on the Microstructure and Mechanical Properties of 2.4 GPa Grade Maraging Steel Fabricated by Laser Powder Bed Fusion. *Addit. Manuf.* **2022**, *59*, 103190. [CrossRef]

44. Böhler AMPO M789. Available online: https://www.bohler-edelstahl.com/en/products/m789-ampo/ (accessed on 5 April 2023).

45. Dehgahi, S.; Ghoncheh, M.H.; Hadadzadeh, A.; Sanjari, M.; Amirkhiz, B.S.; Mohammadi, M. The Role of Titanium on the Microstructure and Mechanical Properties of Additively Manufactured C300 Maraging Steels. *Mater. Des.* **2020**, *194*, 108965. [CrossRef]

46. Deirmina, F.; Davies, P.A.; Casati, R. Effects of Powder Atomization Route and Post-Processing Thermal Treatments on the Mechanical Properties and Fatigue Resistance of Additively Manufactured 18Ni300 Maraging Steel. *Adv. Eng. Mater.* **2022**, *24*, 2101011. [CrossRef]

47. Gorsse, S.; Hutchinson, C.; Gouné, M.; Banerjee, R. Additive Manufacturing of Metals: A Brief Review of the Characteristic Microstructures and Properties of Steels, Ti-6Al-4V and High-Entropy Alloys. *Sci. Technol. Adv. Mater.* **2017**, *18*, 584–610. [CrossRef] [PubMed]

48. Rowolt, C.; Milkereit, B.; Springer, A.; Kreyenschulte, C.; Kessler, O. Dissolution and Precipitation of Copper-Rich Phases during Heating and Cooling of Precipitation-Hardening Steel X5CrNiCuNb16-4 (17-4 PH). *J. Mater. Sci.* **2020**, *55*, 13244–13257. [CrossRef]

49. Fang, R.; Deng, N.; Zhang, H.; Wang, G.; Su, Y.; Zhou, H.; Gao, K.; Gu, L. Effect of Selective Laser Melting Process Parameters on the Microstructure and Properties of a Precipitation Hardening Stainless Steel. *Mater. Des.* **2021**, *212*, 110265. [CrossRef]

50. Kapoor, R.; Batra, I.S. On the A′ to γ Transformation in Maraging (Grade 350), PH 13-8 Mo and 17-4 PH Steels. *Mater. Sci. Eng. A* **2004**, *371*, 324–334. [CrossRef]

51. Schnitzer, R.; Radis, R.; Nöhrer, M.; Schober, M.; Hochfellner, R.; Zinner, S.; Povoden-Karadeniz, E.; Kozeschnik, E.; Leitner, H. Reverted Austenite in PH 13-8 Mo Maraging Steels. *Mater. Chem. Phys.* **2010**, *122*, 138–145. [CrossRef]

52. Höring, S.; Abou-Ras, D.; Wanderka, N.; Leitner, H.; Clemens, H.; Banhart, J. Characterization of Reverted Austenite during Prolonged Ageing of Maraging Steel CORRAX. *Steel Res. Int.* **2009**, *80*, 84–88. [CrossRef]

53. Dossett, J.L.; Totten, G.E. (Eds.) Introduction to Steel Heat Treatment. In *Steel Heat Treating Fundamentals and Processes*; ASM International: Materials Park, OH, USA, 2013; pp. 3–25.

54. Smallman, R.E.; Ngan, A.H.W. Steel Transformations. In *Modern Physical Metallurgy*; Elsevier: Amsterdam, The Netherlands, 2014; pp. 473–498.

55. Peitsch, P.R.; Danón, C.A. Comparative Study of 9% Cr Martensitic-Ferritic Steels Using Differential Scanning Calorimetry. *Procedia Mater. Sci.* **2015**, *9*, 514–522. [CrossRef]

56. Park, J.; Jung, M.; Lee, Y.-K. Abnormal Expansion during the Ferro- to Para-Magnetic Transition in Pure Iron. *J. Magn. Magn. Mater.* **2015**, *377*, 193–196. [CrossRef]

57. Riabov, D.; Frisk, K.; Thuvander, M.; Hryha, E.; Bengtsson, S. Design and Characterization of a Cobalt-Free Stainless Maraging Steel for Laser-Based Powder Bed Fusion. *Mater. Des.* **2022**, *223*, 111180. [CrossRef]

58. Leitner, H.; Schnitzer, R.; Schober, M.; Zinner, S. Precipitate Modification in PH13-8 Mo Type Maraging Steel. *Acta Mater.* **2011**, *59*, 5012–5022. [CrossRef]

59. Sha, W.; Cerezo, A.; Smith, G.D.W. Phase Chemistry and Precipitation Reactions in Maraging Steels: Part IV. Discussion and Conclusions. *Metall. Trans. A* **1993**, *24*, 1251–1256. [CrossRef]

60. Guo, Z.; Sha, W.; Li, D. Quantification of Phase Transformation Kinetics of 18 Wt.% Ni C250 Maraging Steel. *Mater. Sci. Eng. A* **2004**, *373*, 10–20. [CrossRef]

61. De Carvalho, L.G.; Plaut, R.L.; de Lima, N.B.; Padilha, A.F. Kinetics of Martensite Reversion to Austenite during Overaging in a Maraging 350 Steel. *ISIJ Int.* **2019**, *59*, 1119–1127. [CrossRef]

62. Rohrbach, K.; Schmidt, M. Maraging Steels. In *Properties and Selection: Irons, Steels, and High-Performance Alloys*; ASM International: Materials Park, OH, USA, 1990; pp. 793–800.

63. Kaufman, J.G. *Parametric Analyses of High-Temperatures Data for Alluminium Alloys*; ASM International: Materials Park, OH, USA, 2008; ISBN 9780871707154.

64. Maruyama, K.; Abe, F.; Sato, H.; Shimojo, J.; Sekido, N.; Yoshimi, K. On the Physical Basis of a Larson-Miller Constant of 20. *Int. J. Press. Vessel. Pip.* **2018**, *159*, 93–100. [CrossRef]

65. Mittemeijer, E.J. Analysis of the Kinetics of Phase Transformations. *J. Mater. Sci.* **1992**, *27*, 3977–3987. [CrossRef]

66. Gale, W.F.; Totemeier, T.C. (Eds.) Diffusion in Metals. In *Smithells Metals Reference Book*; Elsevier: Amsterdam, The Netherlands, 2004; pp. 13-1–13-120.

67. Moshka, O.; Pinkas, M.; Brosh, E.; Ezersky, V.; Meshi, L. Addressing the Issue of Precipitates in Maraging Steels—Unambiguous Answer. *Mater. Sci. Eng. A* **2015**, *638*, 232–239. [CrossRef]
68. Schnitzer, R.; Zickler, G.A.; Lach, E.; Clemens, H.; Zinner, S.; Lippmann, T.; Leitner, H. Influence of Reverted Austenite on Static and Dynamic Mechanical Properties of a PH 13-8 Mo Maraging Steel. *Mater. Sci. Eng. A* **2010**, *527*, 2065–2070. [CrossRef]